Applied Catalysis A: General 533 (2017) 28–37

Contents lists available at ScienceDirect

Applied Catalysis A: General

journal homepage: www.elsevier.com/locate/apcata

Superior activity of non-interacting close acidic protons in Al-rich Pt/H-*BEA zeolite in isomerization of *n*-hexane

Petr Sazama[a,*], Dalibor Kaucky[a], Jaroslava Moravkova[a], Radim Pilar[a], Petr Klein[a], Jana Pastvova[a,b], Edyta Tabor[a], Stepan Sklenak[a], Ivo Jakubec[c], Lukasz Mokrzycki[a]

[a] J. Heyrovský Institute of Physical Chemistry, Academy of Sciences of the Czech Republic, Dolejskova 2155/3, 182 23 Prague 8, Czech Republic
[b] University of Pardubice, Studentská 95, Pardubice, 532 10, Czech Republic
[c] Institute of Inorganic Chemistry, Academy of Sciences of the Czech Republic, Husinec-Rez, 25068 Rez, Czech Republic

ARTICLE INFO

Article history:
Received 12 October 2016
Received in revised form
15 December 2016
Accepted 17 December 2016
Available online 3 January 2017

Keywords:
Isomerization
Alkanes
Hexane
Zeolites
Al-rich beta (*BEA)
Mordenite

ABSTRACT

Skeletal isomerization of linear alkanes, an essential reaction for the production of gasoline, relies on environmentally questionable chlorinated catalysts, whose activity exceeds that of alternative zeolite catalysts. This work describes an attempt to understand relations between the local arrangement of active sites and skeletal isomerization of *n*-hexane in order to adapt the structure of zeolite catalysts to increase the reaction rates. For this purpose, we used a combination of synthesis of zeolites of *BEA structural topology with unique density and distribution of strongly acid sites, analysis of the nature of the acid sites by ^{1}H MAS NMR spectroscopy and FTIR spectroscopy of the OH groups and adsorbed d_3-acetonitrile, UV–vis-NIR spectroscopy of carbocations formed by protonization, and kinetic analysis. We demonstrate that the high density of non-interacting but close and strongly acidic structural hydroxyl groups significantly lower the activation barrier in the isomerization reaction compared to far-distant acid sites. The organotemplate-free synthesized Al-rich Pt/H-*BEA zeolite (Si/Al 4.2) with an unparalleled high concentration of the non-interacting close H^+ ions balancing the charge of the Al-Si-Al sequences forming a wall between the two channels yields 6 times higher reaction rates compared to state-of-the-art Si-rich Pt/H-zeolite catalysts.

© 2017 Elsevier B.V. All rights reserved.

1. Introduction

Hydroisomerization of linear alkanes into branched alkanes represents a key reaction for the production of automotive fuels. This complex catalytic reaction consists of dehydrogenation of a linear alkane to an alkene on a noble metal, skeletal isomerization of the formed alkene via protonization and a cyclopropyl intermediate on a strongly acidic site and re-hydrogenation of the branched alkene to the alkane (Fig. 1) [1–6]. The dehydrogenation/hydrogenation reactions on a bifunctional catalyst are in thermodynamic equilibrium and practically do not affect the reaction rate of the hydroisomerization [4]. In contrast, the acid-catalysed reaction steps determine the rate of isomerization and require strongly acidic centers [7]. The labile protons of the O—H groups with acid strength strongly enhanced by the presence of chlorine on the traditional chlorinated Pt-alumina catalysts [8] provide sufficient conversion at temperatures as low as 150 °C [9,10]. Since the chlorination occurs by reversible chemical exchange of the surface hydroxyl groups of the alumina support, the use of this catalyst is associated with constant supply and formation of organic chlorines [11], which leads to serious questions about the environmental impact. Zeolite-based acid catalysts, such as Pt-mordenite zeolite with improved texture [12–14] or sulfated Pt-zirconia [15,16] were developed; however, the acid centers of these catalysts facilitate a sufficient rate of isomerization at much higher temperatures. Conversely, low-temperature activity is crucial for achieving sufficient conversion of linear alkanes to branched ones due to the thermodynamic equilibrium of the isomerization reaction, wherein the lower temperatures shift the equilibrium towards the desired di-branched products, whereas higher temperatures hinder their formation. Development of an acidic catalyst for hydroisomerization of linear alkanes, particularly *n*-pentane and *n*-hexane, functional at low temperatures without streams containing low concentrations of chlorine additives, remains a great challenge for heterogeneous catalysis.

Knaeble et al. [7] and Macht et al. [5] documented well that the rate of hexane skeletal isomerization at acid sites with an opened coordination sphere and located in an unconfined space in tung-

* Corresponding author.
E-mail address: petr.sazama@jh-inst.cas.cz (P. Sazama).

http://dx.doi.org/10.1016/j.apcata.2016.12.016
0926-860X/© 2017 Elsevier B.V. All rights reserved.

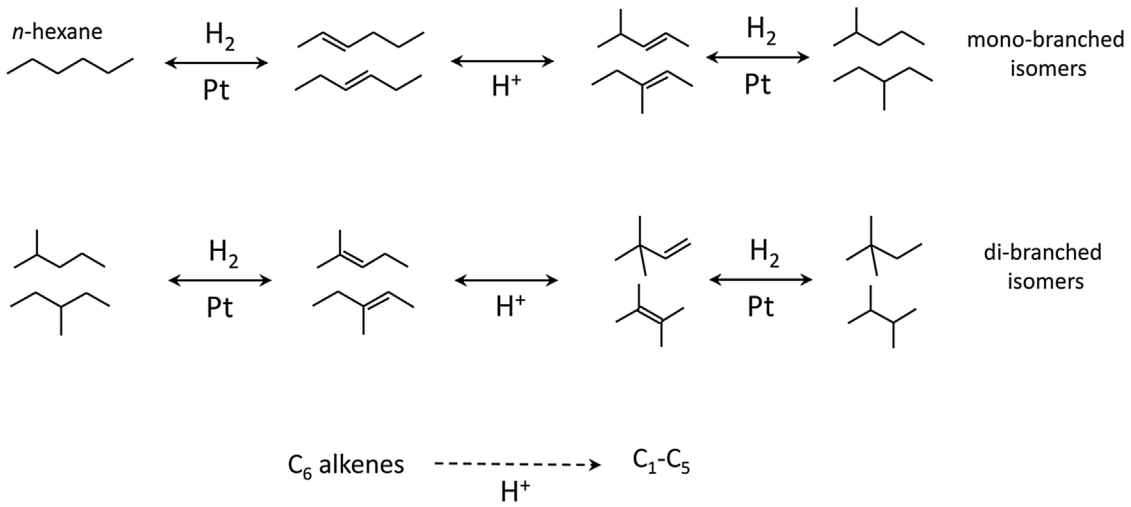

Fig. 1. Reaction scheme for *n*-hexane hydroisomerization on bifunctional Pt/H-zeolite catalysts. The fast dehydrogenation–hydrogenation reactions at Pt sites equilibrate alkanes and all alkene isomers of a given carbon chain structure providing a very low and constant concentration of alkenes. In the acid catalysed reaction steps, the alkene molecules undergo skeletal isomerization and, at high temperatures, also produces lower molecular weight alkanes [5,6].

sten Keggin polyoxometalates supported on silica is proportional to the concentration of acid sites and decreases exponentially with decreasing acid strength. However, in the case of zeolite catalysts, the location of protons in the individual pores of high-silica zeolites and, in addition, the distances between the protons might be also expected to affect their function and reaction pathway in the isomerization reaction. The rate of skeletal isomerization per proton in the 8-member ring (8-MR) side channels of the mordenite structure was reported to be five times higher in comparison with that in the large straight 12-member ring (12-MR) channels [17]. Since the pioneering work of Haag et al. [18], suggesting a linear relationship between the concentration of tetrahedral aluminum in the framework, hence the acid centers, and the reaction rate in the cracking of hexane, it has been well established that, not only the concentration, but also the local spatial arrangement of acidic centers attached to crystallographically different sites in the channels [19,20] and the distance between them [21] fundamentally influence both the reaction rate and the mechanism.

In pursuing the present work on the isomerization of linear alkanes over zeolites, we wanted to specify the role of an increase in the density of the strongly acidic protons countering the negative charge of the framework in the H-forms of zeolites in relation to the occurrence of Al-Si-Al sequences, inevitably formed at high concentration of Al in the zeolite framework. We wanted to determine the effect of variations in the distribution of aluminum providing charge balance for the corresponding high concentration protons located in the close vicinity on the reaction rate and selectivity. We therefore employed zeolite *BEA topology, which can be prepared in a broad range of Al concentrations and which offers fast intra-crystalline diffusion of reactants and products through channels with three-dimensional architecture and 12-MR openings. We exploited recent progress in the synthesis of the beta zeolite that opened a new potential to manipulate the framework aluminum content in a very broad range and employed Al-rich beta zeolites with very high concentration of aluminum (Si/Al ≥ 4) with highly predominant tetrahedrally coordinated Al in the framework [22–34]. This approach enabled us to examine the extent to which the isomerization reaction is affected by close proximity of strongly acidic centers. We found that the high density of non-interacting strongly acidic sites facilitates extraordinarily high reaction rates due to a synergetic effect significantly decreasing the activation barrier of the reaction. This enabled more rational design of isomerization zeolite catalysts providing superior activity.

2. Experimental

2.1. *BEA and MOR zeolites and preparation of Pt/H-catalysts

Al-rich beta zeolite (molar Si/Al 4.2), denoted as *BEA/4.2, was hydrothermally synthesized from aluminosilicate synthesis gel prepared from $NaAlO_2$ and fumed silica (Cabosil) in the absence of an organic structure-directing agent and using seeding of calcined beta crystals (TZB-212, Tricat). Details of the procedure were reported previously [33]. The high-silica zeolites used as standards for comparing the catalytic properties kindly supplied by the Tricat Company (now part of Clariant), (*BEA, Si/Al 11.5, TZB-212) and Zeolyst International (*BEA, CP814B-25, Si/Al 12.5 and MOR, CBV 20A, Si/Al 12.1) were denoted as *BEA/11, *BEA/12, and MOR/12, respectively. A hierarchical mordenite zeolite with optimal micro-mesoporous structure was prepared and used for comparing the catalytic properties of Al-rich beta zeolite with a state-of-the-art hydroisomerization zeolite-based catalyst [12]. The hierarchical mordenite was prepared by treatment of MOR/12 in alkaline solutions (30 ml 0.2 M NaOH per 1 g mordenite stirred in a beaker at 85 °C for 2 h) and subsequently in acid solution (10 ml 0.1 M oxalic acid per 1 g alkaline treated zeolite stirred in a beaker at 85 °C for 20 h). All the zeolites were ion-exchanged with 0.5 mol dm^{-3} NH_4NO_3 at RT (1 g of a zeolite per 100 cm^3 of solution, three times over 12 h).

Pt was introduced into the zeolites by incipient wetness impregnation of pre-dried (105 °C/2 h) powder zeolites with a H_2PtCl_6 solution to yield 1.5 wt.% of Pt. The Pt-impregnated granulated zeolite was activated before the catalytic test in a stream of O_2 at 450 °C for 3 h, then purged by a N_2 stream at 450 °C, then cooled down to 250 °C, and finally activated in a mixture of 80 mol% H_2 and 20 mol% N_2 at 250 °C for 1 h.

2.2. Structural analysis

X-ray powder diffraction (XRD) patterns were obtained with a graphite monochromator and a position sensitive detector (Våntec-1) using a Bruker AXSD8 Advance diffractometer with CuKα radiation in Bragg–Brentano geometry. The porosity of the zeolites was determined by the analysis of the adsorption isotherms of nitrogen at 77 K carried out using an ASAP2010 apparatus (Micromeritics). Before the adsorption experiment the samples were outgassed at 240 °C for at least 24 h. The crys-

tal morphology and the Pt dispersion were analyzed using a scanning electron microscope (SEM, JEOL JSM-5500LV) and a high-resolution transmission electron microscope (HR-TEM, JEOL JEM 3010), respectively. The chemical compositions of the parent and prepared Pt-zeolites were determined by X-ray fluorescence spectroscopy using a PW 1404 (Philips). A Nicolet Nexus 670 FTIR spectrometer was used to collect the FTIR spectra of the H-forms of zeolites. The samples in the form of a self-supporting wafers were activated at 450, 500 and 550 °C in a dynamic vacuum for 3 h in-situ in the IR cell. CD_3CN was adsorbed at a partial pressure of 13 mbar at RT for 20 min and then evacuated for 15 min at RT. The spectrometer with a MCT-B detector was operated at 1 cm^{-1} resolution and 256 scans were averaged for one spectrum. The intensity of the absorption bands was normalized using the bands of the overtone vibrations of the zeolite lattice as an internal standard. The spectra in the stretching vibration of C≡N were processed by deconvolution and curve fitting by the procedure according Wichterlova et al. [35] to obtain the integral area of the band characteristic of the Brønsted and Lewis sites. The extinction coefficients ε_B = 2.05 cm μmol^{-1} and ε_L = 3.60 cm μmol^{-1} were used for calculations of the corresponding concentrations of acid sites. Solid state ^1H and ^{29}Si MAS NMR experiments were carried out on a Bruker Avance 500 MHz Wide-Bore spectrometer (11.7 T) equipped with 4 mm double-resonance MAS NMR probe-head. ^1H MAS NMR single pulse spectra were collected after 128 scans with a $\pi/2$ (4 μs) excitation pulse and 2 s repetition delay at a rotation speed of 11 kHz. To obtain the protonic form (H-*BEA), "parent" NH_4-*BEA samples were dehydrated *in-situ* in 4 mm ZrO_2 MAS NMR rotors at 450 °C (ramp 1 °C.min^{-1}) under dynamic vacuum of 5.10^{-1} Pa for 6 h. ^{29}Si MAS NMR single pulse spectra of hydrated zeolites were measured at a rotation speed of 7 kHz, with a $\pi/6$ (1.7 μs) excitation pulse and relaxation delay of 30 s for single pulse spectra. The framework aluminum content (Si/Al_{FR}) was estimated from the intensity of the ^{29}Si NMR spectra according to Refs. [36,37]. The UV–vis spectra of Al-rich and Si-rich H-*BEA zeolites dehydrated at 500 °C in a vacuum after interaction with hexamethylbenzene (HMB) at 200 °C for 1, 2 and 3 h and after subsequent interaction with NH_3 were measured in the range from 20 000 to 45 000 cm^{-1} using a Perkin-Elmer Lambda 950 spectrometer equipped with a Spectralon integration sphere. HMB was introduced into the dehydrated zeolite by mixing the powdered zeolite and HMB in a glovebox and the measurements were performed using a cell enabling collection of the spectra without exposure of the mixture to the air.

2.3. Kinetic analysis

The kinetic analysis of hydroisomerization of *n*-hexane to the corresponding *iso*-hexanes was performed in a regime implying equilibrium between hydrocarbons in the micropores and gas phase reached by a high H_2/hydrocarbon molar ratio and correspondingly low concentration of hexanes in the reaction stream [38]. The kinetic regime under the reaction conditions was confirmed by variation in the total gas flow and the weight of the catalyst. Small crystallites of the zeolites (~0.05–0.4 μm) guaranteed the absence of intra-crystalline diffusion constraints to the overall reaction rates as the internal diffusion limitations have been shown to be irrelevant for crystal sizes at least up to 12 μm for both the *n*-hexane hydroisomerization [38] and cracking [39]. The concentration of platinum of 1.5 wt.% in the prepared Pt-zeolite catalysts provides a sufficient rate of (de)hydrogenation reactions yielding hexene/hexane in equilibrium and not limiting the overall alkane hydroisomerization [38]. The catalytic tests were carried out in a glass flow-through tubular U-shaped reactor under atmospheric pressure. 0.50 g of a catalyst and the reaction stream consisting of 79 mol.% H_2, 20 mol.% N_2 and 1 mol.% of *n*-hexane kept at a total flow rate 66 cm^3 min^{-1} corresponded to WSHV 0.25 h^{-1} and GHSV 4000 h^{-1}. The temperature of the reactor was controlled with an internal thermocouple and kept at the desired temperature in the range 125–250 °C. The concentrations of *n*-hexane, branched hexanes and lower molecular weight products (methane, ethane, propane, butane, and *iso*-butane) were analyzed by an on-line connected Finnigan 9001 gas chromatograph equipped with a 50m × 0.32mm × 5 μm Al_2O_3/KCl capillary column and an FID detector. Steady-state conditions were achieved within 0.5–3 h of reaction time-on-stream. The reaction rates of the *n*-hexane to *iso*-hexane were calculated at low conversion values and close to 100% selectivity for *iso*-hexanes. Only the conversion values <6% are considered for our calculation of the reaction rates ($mol_{iso\text{-}hexanes}$ g_{cat}^{-1} s^{-1}) and the TOF values for the reaction per Al ($mol_{iso\text{-}hexanes}$ mol_{Al}^{-1} s^{-1}).

The conversions and yields of branched hexane isomers and lower molecular weight by-products were also analyzed under process-like conditions. These catalytic tests were performed using a stainless-steel gas flow tubular PID Eng&Tech Microactivity – Reference reactor at a pressure of 10 bar with a H_2 to hexane molar ratio of 6 and amount of catalyst equal to 2.5 g (5 ml) with a flow rate corresponding to WHSV 0.7 h^{-1} and GHSV 638 h^{-1}. The temperature was controlled by an internal thermocouple and kept at the desired temperature in the range 200–215 °C. Liquid *n*-hexane was continuously loaded by a Gilson 307 pressure pump and evaporated in the hot flow of hydrogen gas. The reaction products were analyzed using an on-line connected Perkin Elmer Clarus 580 gas chromatograph equipped with CP-Sil Pona CB column (100 m × 0.25 mm × 0.5 μm) and a FID detector.

3. Results and discussions

An optimized organotemplate-free hydrothermal synthesis was employed for the preparation of the Al-rich *BEA zeolite (molar Si/Al 4.2). Its structural as well as acid and catalytic properties were examined in detail to compare with the high-silica *BEA zeolite (molar Si/Al 11.3) to obtain an insight into the nature and role of the high density of acid sites in hydroisomerization of *n*-hexane.

Commercial high silica zeolites of *BEA and MOR structure with the molar Si/Al 12.5 and 12.1, respectively, and a hierarchical mordenite zeolite (molar Si/Al 9.5) with optimal micro-mesoporous were further used to demonstrate the functionality of the Al-rich *BEA zeolite in the hydroisomerization reaction in comparison with a state-of-the-art hydroisomerization zeolite-based catalyst. The main characteristics of the *BEA and MOR zeolites are listed in Table 1.

3.1. Physicochemical characterization

The patterns of the X-ray diffraction lines are characteristic for the beta and mordenite zeolites without impurity phases (Fig. 2A). The high intensities of the X-ray diffraction lines and the absence of a diffuse halo peak indicate a well-developed crystalline structure without the presence of an amorphous phase. The representative SEM image shows that the Al-rich *BEA/4.2 sample consists of well-developed intergrown crystals with a uniform morphology of partially truncated octahedrons with an average size of ~0.4 μm (Fig. 2D). The N_2 sorption isotherm of the *BEA/4.2 sample is characteristic of purely microporous material (Type I, isotherm profile), with a high microporous volume and the apparent surface area of 510 m^2 g^{-1} (Table 1). The *BEA/11 and *BEA/12 samples consist of very small crystallites with an average size of ~0.05 and ~0.1 μm, respectively. Analysis of the adsorption isotherms (Fig. 2B) showed high apparent surface areas of 617 and 605 m^2 g^{-1} for *BEA/11 and *BEA/12, respectively, and a high adsorption on the external surface of the small crystallites at higher relative pressures. The SEM image

Table 1
Characteristics of the beta ([*]BEA) and mordenite zeolites.

Sample	Zeolite	Si/Al[a]	Si/Al$_{FR}$[b]	c_{Al}[a] mmol g^{-1}	c_B[c] mmol g^{-1}	c_L[c] mmol g^{-1}	Crystal size μm	S m^2 g^{-1}
H-[*]BEA/4.2	Al-rich [*]BEA	4.2	4.7	3.0	1.80	0.22	~0.4	510
H-[*]BEA/11	Si-rich [*]BEA	11.3	11.5	1.4	0.63	0.32	~0.05	617
H-[*]BEA/12	Si-rich [*]BEA	12.5	15.0	1.2	0.48	0.30	~0.1	605
H-MOR/12	Si-rich MOR	12.1	12.5	1.3	1.06	0.11	~0.15	454
H-MOR/10	Micro-mesoporous Si-rich MOR	9.5	11.2	1.6	0.77	0.35	~0.15	405[d]

[a] From chemical analysis of the Na^+ form of zeolites.
[b] From ^{29}Si MAS NMR spectra of the Na^+ form of zeolites.
[c] Concentration of Brønsted and Al-Lewis sites from FTIR spectra of adsorbed d_3-acetonitrile on the H^+ form of zeolites.
[d] External surface area 110 m^2 g^{-1}.

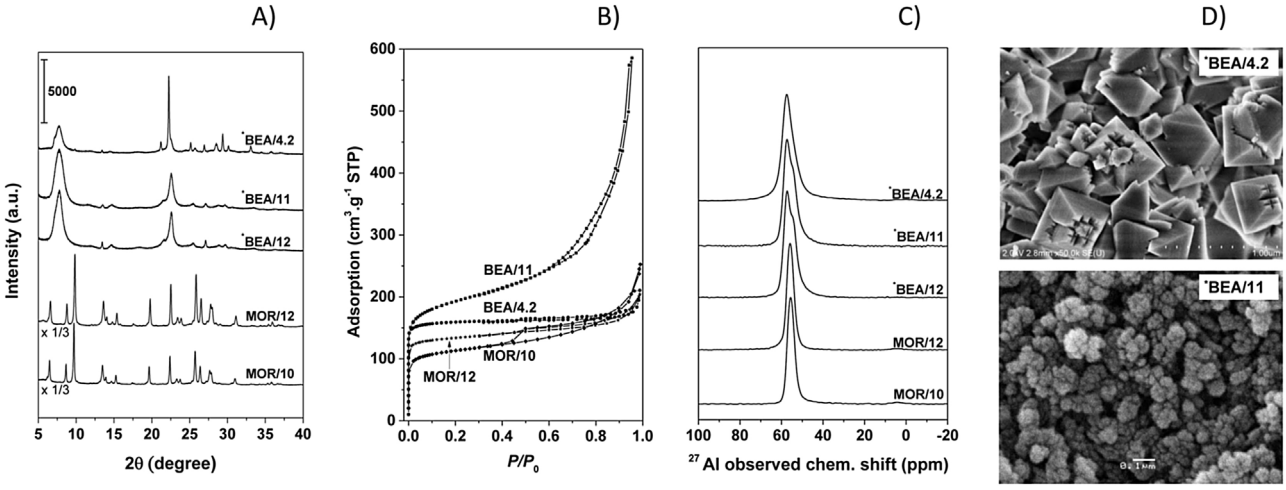

Fig. 2. A) X-ray powder diffractograms, B) adsorption isotherms of N_2 at 77 K, C) ^{27}Al MAS NMR spectra, and D) SEM images of the [*]BEA and MOR zeolites.

of the microporous MOR/12 (Fig. S1) shows aggregated crystals of an average size of ~0.15 μm and the HR-TEM image of its micro-mesoporous analogue MOR/10 exhibits the presence of a secondary mesoporous structure characterized by numerous cavities about 5–20 nm in size (Fig. S1). The XRD patterns are slightly broadened for the micro-mesoporous mordenite compared to the microporous analogue indicating a smaller effective crystallite size of the zeolite. The adsorption isotherm of MOR/12 is typical for a purely microporous zeolite while the MOR/10 zeolite exhibits an adsorption in the zeolite micropores and a hysteresis loop typical for mesopores with the mesoporous surface area of 110 mg^{-1} (Table 1). ^{27}Al MAS NMR spectra of all the investigated zeolites show the absence of a signal at 0 ppm and the presence of a strong resonance envelope with the chemical shift of about 55 ppm reflecting the tetrahedral coordination of Al atoms (Fig. 2C). The tetrahedral coordination of Al atoms is consistent with comparable values of the framework Si/Al$_{FR}$ ratios obtained using analysis of the ^{29}Si MAS NMR spectra and those obtained from the chemical analysis (Table 1).

3.2. Analysis of acid sites

The pair of samples H-BEA/4.2 and H-BEA/11 zeolites, exhibiting different concentration of the framework Al atoms corresponding to molar Si/Al$_{FR}$ 4.7 and 11.5, respectively (Table 1), was analyzed for the concentration and strength of the Brønsted sites, the concentration of Lewis acid sites and the presence of structural defects using ^{1}H MAS NMR spectroscopy, FTIR spectroscopy of the OH groups and adsorbed d_3-acetonitrile, and UV-VIS-NIR spectroscopy of carbocations formed by protonization upon adsorption of hexamethylbenzene (HMB). The ^{1}H MAS NMR spectra of the dehydrated H-[*]BEA/4.2 and H-[*]BEA/11 zeolites (Fig. 3A) exhibit bands with maxima at 1.6, 2.0, 2.4–2.5, and 3.6–3.8 ppm characteristic of terminal and internal SiOH, extra-framework AlOH and bridging Si(OH)Al groups, respectively [40,41]. The main difference in the spectra of H-[*]BEA/4.2 and H-[*]BEA/11 is in the intensity of the signal characteristic of bridging Si(OH)Al groups. The 3 times higher intensity of the signal of the Brønsted sites for H-[*]BEA/4.2 corresponds to the increase in the concentration of Al in the zeolite with Al atoms incorporated predominantly in the regular T_d coordination in the framework. The close positions of the band maxima at 3.6 and 3.8 ppm for Si- and Al-rich [*]BEA, respectively, can indicate that the acid strength does not greatly differ. The maxima of the signals of the OH groups in the zeolites are not unambiguously connected with their acid strengths; however, the shift matches the changes in properties for a single zeolitic structure [42,43]. The signal of silanol groups forming a surface termination of the crystalline structure is weak for H-[*]BEA/4.2 due to the low external surface of well-developed crystallites compared to high intensity of the band for [*]BEA-11 characteristic of small crystallites. It is obvious that the signal of the internal silanol groups reflecting structural defects associated with removal of the T-atoms or intergrowth structure also exhibits barely distinguishable intensity for the Al-rich [*]BEA sample compared to the Si-rich [*]BEA. As the intensities of the ^{1}H MAS NMR bands do not depend on the band positions, they accurately reflect the ratio between the concentrations of the individual hydroxyls. Thus the low intensity signal of the internal silanol groups and the low signal of the OH groups bound to extra-framework and/or perturbed framework Al atoms indicate that the Al-rich [*]BEA/4.2 sample has a well-developed low-defective crystalline structure.

Fig. 3B and C show the FTIR spectra in the region of hydroxyl group vibrations of H-[*]BEA/4.2 and H-[*]BEA/11 evacuated at temperatures from 450 up to 550 °C and after adsorption of d_3-acetonitrile, respectively. The FTIR spectra in the region of the

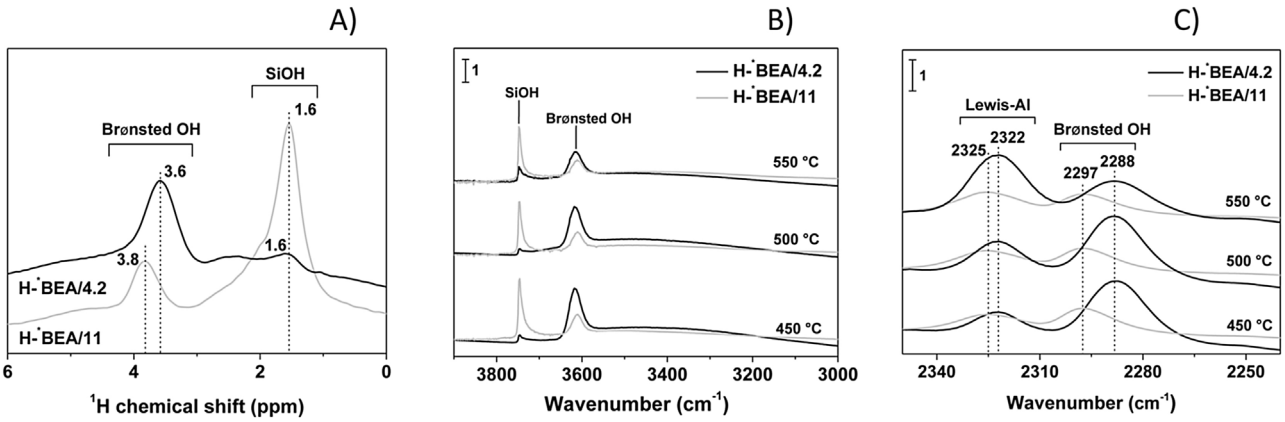

Fig. 3. Analysis of acid sites in H-*BEA zeolites. A) ^{1}H MAS NMR spectra of H-*BEA zeolites dehydrated at 500 °C, and FTIR spectra for zeolites dehydrated at increasing temperatures in B) the region of the $\nu_{0\rightarrow1}$OH vibration and C) in the region of the $\nu_{0\rightarrow1}$C≡N vibration after adsorption of d_3-acetonitrile.

hydroxyl group exhibit approximately 3 times higher intensity of the bands with maxima at about 3610–3613 cm^{-1} of the stretching vibration of the bridging hydroxyls, negligible intensity of the bands at 3650–3660 cm^{-1} of perturbed framework or extra-framework AlOH [44–46] and low intensity of the band at 3727–3745 cm^{-1} of silanols for the H-*BEA/4.2 sample compared to H-*BEA/11 in good agreement with the ^{1}H MAS NMR results. Only evacuation at 550 °C produced a considerable loss of the intensity for the bridging hydroxyls. This indicates sufficient structural stability of Al-rich H-*BEA zeolite at temperatures relevant for the isomerization reactions. Adsorption of d_3-acetonitrile resulted in the appearance of the bands at 2325 and 2297 cm^{-1} corresponding to the stretching mode of ν(C≡N) of d_3-acetonitrile adsorbed on Lewis and Brønsted sites, respectively [35]. Quantitative analysis of the acid sites using the integral intensities of the IR bands and the extinction coefficients for the C≡N group interacting with the Brønsted and Lewis sites [35] indicated a slightly predominant concentration of Brønsted sites compared to concentration of Lewis sites in the H-*BEA/4.2 sample (Table 1). The formation of a significant concentration of Lewis sites is connected with a reversible change in the coordination of the framework Al atoms characteristic of the structure of the *BEA zeolite [34,47–52] and also observed for Al-rich *BEA [53]. Thus the ^{1}H MAS NMR and FTIR spectra and OH groups and adsorbed d_3-acetonitrile together show that the increase in the concentration of the aluminum content does not led to significantly increased dehydroxylation and formation of Lewis acid sites and the concentration of Brønsted hydroxyls in Al-rich beta zeolite is proportional to the increase in the concentration of Al in the zeolite framework.

The ability of the Brønsted hydroxyls to protonate hexene, the essential step in the isomerization reaction, is controlled by interplay of the concentration and strength of the acidic centers and confinement of the hydrocarbon molecule in a constrained environment of the zeolite channels [17]. However, the protonation of hexene cannot be experimentally followed because of the unmeasurable hexene concentration under realistic reaction conditions and at higher concentrations due to the rapid oligomerization of the akenes and the formation of complex hydrocarbon molecules [54]. Therefore, the ability of Al-rich H-*BEA zeolite to form carbenium ions was analyzed using the hexamethylbenzene (HMB) molecule, whose protonation yields the relatively stable hexamethylbenzenium cation providing electronic transitions with characteristic spectral components in the range of UV–vis light [55]. The UV–vis spectra of HMB and carbocations formed by protonization of adsorbed hexamethylbenzene (HMB) in Al-rich and Si-rich H-*BEA zeolites are shown in Fig. 4. The UV–vis spectrum of neutral HMB exhibited a typical absorption band at 37 000 cm^{-1} characteristic of the π-electron system of the aromatic ring [56]. Adsorption of HMB in both Si- and Al-rich *BEA zeolites resulted in the appearance of an intense band with maximum at 25 500 cm^{-1} with a shoulder around 29 500 cm^{-1} corresponding to the formation of the hexamethylbenzenium cation [55,57]. The spectra obtained for the two zeolites do not show significant differences in the positions and shapes of the high intensity bands of the carbenium ions and are very similar to those of protonated benzene in a superacidic solution [56]. The assignment of the bands to the hexamethylbenzenium cation was demonstrated experimentally by co-adsorption of ammonia, resulting in disappearance of the band at 25 500 cm^{-1} consistent with proton transfer between ammonia as a stronger base and the hexamethylbenzenium cation forming the ammonium ion and neutral HMB.

3.3. Nature and local arrangement of acid sites in Al-rich H-*BEA

The negligible intensity of the internal silanol groups, the low signal of the OH groups bound to extra-framework and/or perturbed framework Al atoms and very high intensity of the structural bridging OH groups observed in the ^{1}H MAS NMR and FTIR spectra of Al-rich H-*BEA are characteristic of a non-defective crystalline structure with a high concentration of non-interacting (isolated) acid sites associated with tetrahedrally coordinated Al atoms in the zeolite framework. Consistently, the distinctively ordered nature and essentially defect free structure for Al-rich H-*BEA were reported by Yilmaz et al. [58] and Sasaki et al. [59]. In Al-rich *BEA zeolites (Si/Al 4–5), the Al atoms are predominantly present in the Al-Si-Al sequences [29,33,53,60,61] with the concentrations of Al-Si-Al ranging from 40% to 100% of the total Al depending on their arrangement in rings or as long sequences [53]. It follows that the majority of the H^{+} ions in the H-*BEA/4.2 sample compensate the negative charge resulting from substitution of the framework Si(IV) by Al(III) in the Al-Si-Al sequences; however, the respective OH groups are reflected in the ^{1}H MAS NMR and FTIR spectra as non-interacting OH groups. Our previous ^{27}Al and ^{29}Si (CP) MAS NMR studies supplemented by FTIR of adsorbed d_3-acetonitrile and UV–vis spectroscopy of Co(II) ions as probes of close Al atoms and further supported by DFT molecular dynamic calculations of the Co(II) sites in the *BEA zeolites revealed that these Al-Si-Al sequences in Al-rich *BEA zeolites are mostly located in the zeolite wall separating two channels and the Al atoms of the sequence thus face two channels (see Fig. 5 and Ref. [53]). The negative charge of the framework originating from these sequences is balanced by two H^{+} ions located in different channels. Therefore the high concentration of Al atoms in the framework of Al-rich beta zeolites does not result in increased formation of interacting OH

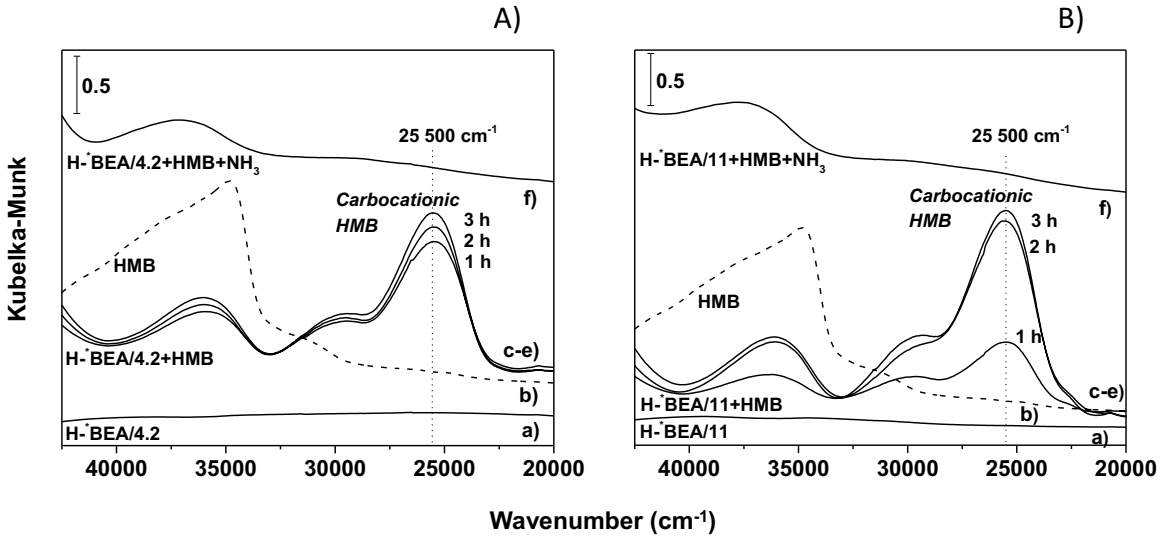

Fig. 4. UV-vis spectra of carbocations formed by protonization of hexamethylbenzene (HMB) in A) Al-rich and B) Si-rich H-*BEA zeolites. Spectra of a) zeolites dehydrated at 500 °C, b) solid HMB, c–e) zeolite after interaction with HMB at 150 °C for 1, 2 and 3 h, respectively, and f) after subsequent interaction with NH_3.

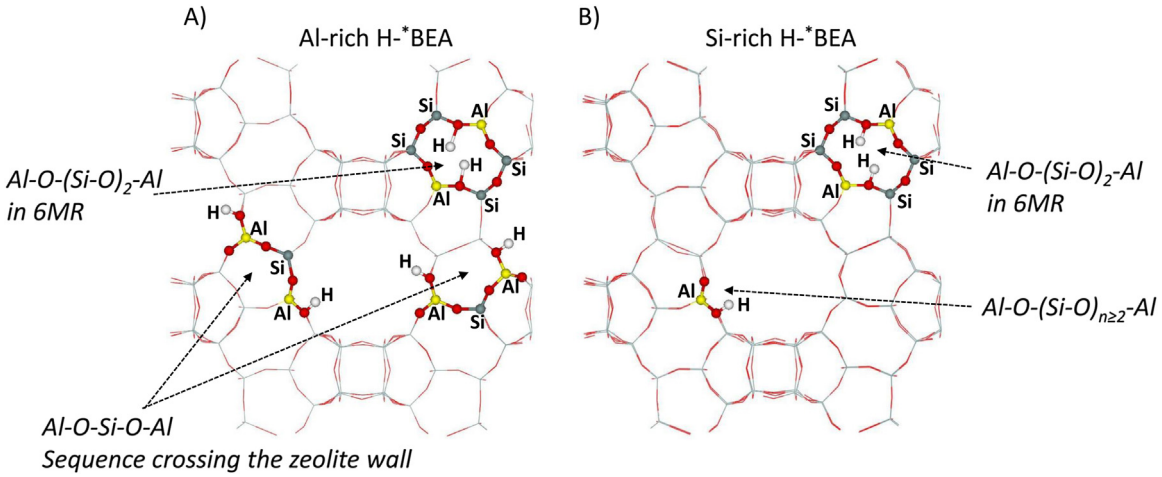

Fig. 5. Schematic representations of the main Al-O-$(SiO)_n$-Al sequences in A) Al-rich and B) Si-rich H-*BEA zeolites. H^+ compensates the charge mainly from Al-O-Si-O-Al sequences in Al-rich H-*BEA whereas the closest Al atoms form an Al-O-$(SiO)_2$-Al sequence in Si-rich H-*BEA. The Al-O-Si-O-Al sequences cross the zeolite wall and the corresponding H^+ are located in two different channels in Al-rich H-*BEA. Oxygens in red.

groups but the Al-Si-Al sequences forming the zeolite beta wall provide H^+ sites like in a Si-rich zeolite but in significantly increased concentrations. The calculated deprotonation energies used as a measure of the acid strengths of the Brønsted sites corresponding to AlSiAl and AlSiSiAl sequences in Al- and Si-rich *BEA, respectively, reported in the previous study [33], were in the range of differences in the deprotonation energy values among the protons associated with AlOHSi groups at individual T sites in the framework of *BEA zeolites. This is consistent with the small observed shift in the maxima of the band of bridging hydroxyl groups in the ^{1}H MAS NMR and FTIR spectra, and the similar protonating ability of HMB molecules. Suganuma et al. [62] assessed the Brønsted acid strength and related acidic property of Al-rich H-*BEA zeolites using analysis of the enthalpy of ammonia desorption combined with FTIR measurements. The enthalpy distributed mainly in the range between 115 and 145 kJ mol^{-1} demonstrated that the Al-rich H-*BEA is a strongly acidic zeolite, essentially having the acid strength in the region generated by isomorphous substitution of Si by Al in the common *BEA framework [62]. Similarly, De Baerdemaeker et al. [29] deduced the presence of a large amount of remarkably strong acid sites from the amount and the temperature at which the NH_3 desorbs from Al-rich H-*BEA. The pair of Al- and Si-rich H-*BEA zeolites thus represents unique material that allows elucidation of the effect of the close vicinity of non-interacting acidic protons on activation of a hydrocarbon molecule in acid-catalysed reactions over zeolite catalysts, moreover, in the three-dimensional channel system with 12-MR openings providing easy intra-crystalline diffusion of reactants and products.

3.4. *The effect of the density of acid sites on* n*-hexane hydroisomerization*

Fig. 6 depicts the yields of branched hexanes and low molecular products as a function of temperature and Arrhenius plots for hydroisomerization of *n*-hexane over Al- and Si-rich Pt/H-*BEA zeolites. The high concentration of close strongly acidic sites in Al-rich *BEA led to a significantly improved yield of branched isomers with very low yield of undesired C_1–C_5 products compared Si-rich *BEA zeolites over the entire temperature range from 125 to 225 °C. The high density of Brønsted sites facilitated increased conversion of *n*-hexane to *iso*-hexane from 5.9 to 35.5% practically without formation of side-products (0.2% yield of C_1–C_5) at 175 °C

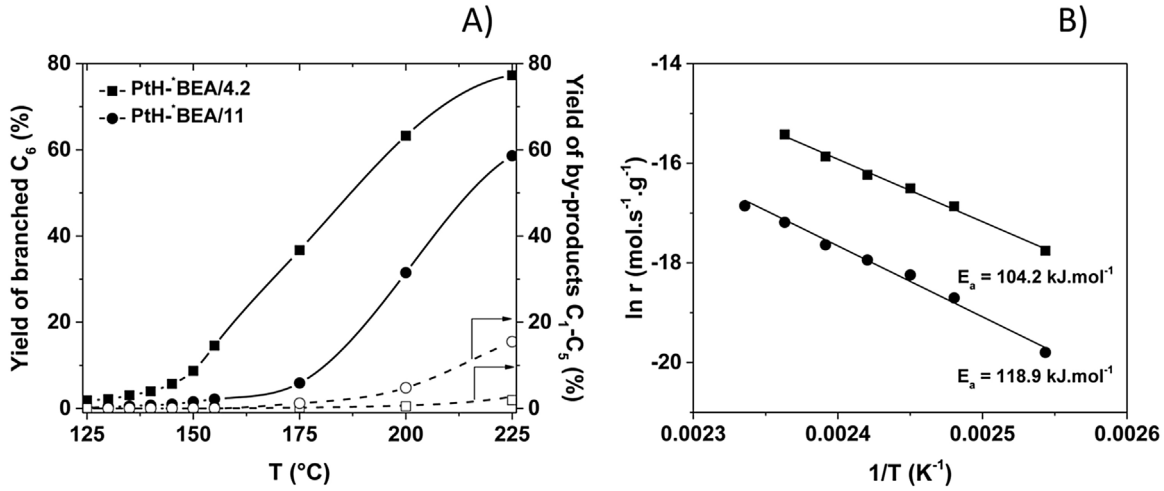

Fig. 6. Hydroisomerization of *n*-hexane over Al-rich *BEA (PtH-*BEA/4.2) compared with Si-rich *BEA zeolite (PtH-*BEA/11). A) Effect of temperature on the yields of branched C_6 isomers and C_1–C_5 by-products and B) Arrhenius plot. Reaction conditions: WHSV 0.25 h^{-1}, molar ratio H_2/n-C_6 79, atmospheric pressure.

Table 2
Hydroisomerization of *n*-hexane to 2-methyl- and 3-methylpentanes, reaction rates (r_{ISO}) and turnover frequencies (TOF) for 145 °C.

Sample	[a]$y_{iso\text{-}C6}$ %	r_{iso} molng^{-1} s^{-1}	[b]TOF s^{-1}
PtH-BEA/4.2	5.68	5.7 10^{-8}	1.8 10^{-5}
PtH-BEA/12	0.99	9.8 10^{-9}	8.1 10^{-6}

Reaction conditions: WHSV 0.25 h^{-1}, molar ratio H_2/n-C_6 79, atmospheric pressure.
[a] Yield of 2-methyl- and 3-methylpentanes while the formation of di-branched hexane isomers and lower molecular weight by-products was negligible.
[b] TOF calculated for total concentration of Al.

(Table S1). The reaction rate per gram of Al-rich *BEA zeolite, calculated at low conversions of *n*-hexane, high selectivity for 2-methyl- and 3-methylpentanes (>95%), low selectivity for di-branched hexane isomers (<5%), and negligible selectivity for lower molecular weight by-products (<0.1%), exceeds six fold that of Si-rich *BEA (Table 2). More than twice higher TOF calculated per total concentration of Al for Al-rich *BEA clearly shows the substantially higher specific activity of the active sites. The remarkable improvement in the catalytic performance is reflected in the lower apparent activation energy of 104.2 vs. 118.9 kJ mol^{-1} obtained from the Arrhenius plots for Al- and Si-rich *BEA, respectively, in accordance with the higher specific activity of the active sites. The six-fold higher reaction rate, higher TOF and the lower apparent activation energy by ca. 15 kJ mol^{-1} for Al-rich *BEA zeolite clearly indicate a synergistic effect of the high concentration and close proximity of the OH groups.

3.5. *Effect of platinum on* n-*hexane hydroisomerization*

A sufficient concentration of functional clusters of metallic platinum is essential for ensuring the dehydrogenation/hydrogenation reactions not limiting the overall alkane hydroisomerization on the bifunctional Pt-zeolite catalysts [38,63]. Ribeiro et al. [63] showed that the hydrogenation-dehydrogenation reaction was much faster than the skeletal isomerization on acid centers and the isomerization did not depend on the surface of the metal for the metal loading from 0.5 to 6 wt.% of dispersed Pt on the faujasite zeolite. Van de Runstraat demonstrated that the metal function was not rate determining for Pt-*BEA with the metal loading ~1.5 wt.% Pt. For our study, all the Pt-zeolites were prepared with a concentration of 1.5% Pt. The platinum dispersity in the prepared zeolites was checked by HR-TEM and a CO sorption followed by FTIR spectroscopy measurements. HR-TEM images of all the prepared samples (Fig. S2) showed the presence of well-dispersed platinum clusters located on the external surface of zeolite crystals with a wide distribution of particle sizes ~1–20 nm. However, we cannot exclude the presence of platinum also in the zeolite channels. The comparison of the absorption bands in the FTIR spectra in the region of hydroxyl group before and after Pt introduction into Si- and Al-rich H-*BEA zeolites indicated only very small changes in the intensity of the bridging OH groups (not shown). This indicates that the Pt species are not coordinated into cationic sites in a significant extent after the reduction of Pt in a hydrogen atmosphere. The oxidation state and nature of the platinum species located inside the zeolite channels and the outer surface was analysed using the FTIR spectra of CO adsorbed on the Al-rich Pt/H-*BEA compared with the Si-rich Pt/H-MOR and the Pt/H-*BEA zeolites (Fig. 7). The positions of the FTIR absorption bands of adsorbed CO on Pt^{2+} counterions charge balanced by the zeolite framework, $Pt_n^{\delta+}$ clusters, and reduced Pt metallic clusters were reported at 2170–2150 cm^{-1}, 2130–2140 cm^{-1}, and 2050–2100 cm^{-1}, respectively [64,65]. The analysis of the spectrum of Al-rich Pt/H-*BEA reveals the presence of a major absorption band at 2078 cm^{-1} characteristic for reduced Pt metallic clusters of 1–20 nm in size [64,65] located on the external surface of zeolite crystal without the presence of any unusual absorption bands. The absence of a significant absorption intensity at about 2170–2130 cm^{-1} indicates a reduction of Pt into the zero-valent oxidation state of metallic Pt in the Al-rich Pt/H-*BEA zeolite. The broad intensity of the band reflects the presence of platinum species of non-uniform sizes which is typical for Pt introduced by an impregnation method. The representative HR-TEM image of Pt/H-*BEA/4.2 shows well-dispersed cubic and tetrahedral Pt-nanoparticles located on the external interior of zeolite crystals with a wide distribution of particle sizes ~1–20 nm (Fig. 7B). The spectrum of adsorbed CO on Si-rich Pt/H-*BEA exhibits compared to Al-rich Pt/H-*BEA higher intensity of the band at about 2080 cm^{-1} indicating a better dispersion of Pt on the large external surface of small crystals of Si-rich Pt/H-*BEA. These results are consistent with the observations that the reactions occurring on Pt for high metal loadings (~1% Pt) are much faster than on acid sites and the rate of hydroisomerization is independent of the metal area of dispersed Pt clusters [63,66]. Thus Pt dispersed in the form of metallic clusters can provide sufficient functionality regardless of the specifics of their structure for all the Pt/H-zeolite catalysts.

To further analyse whether the activity of the Al-rich Pt/H-*BEA zeolite could also be associated with the specificity of Pt

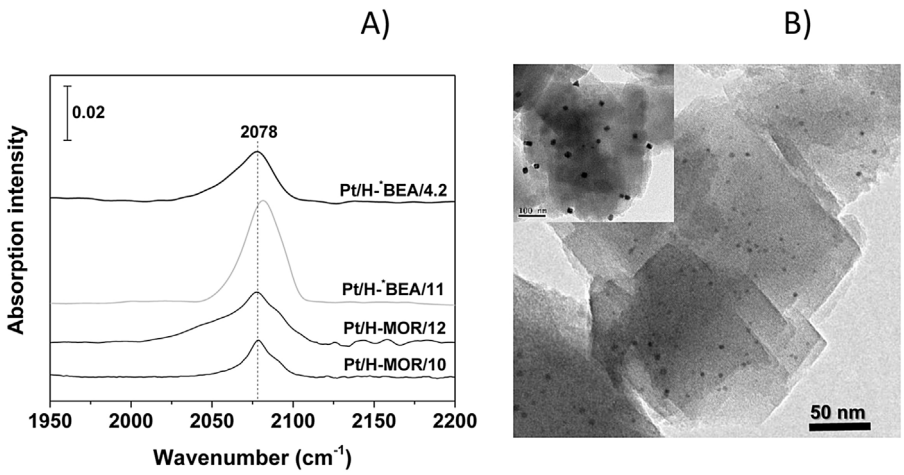

Fig. 7. Analysis of Pt in Pt/H-zeolites. A) FTIR spectra of CO adsorbed on the Pt/H-zeolites reduced by hydrogen at 250 °C and B) the representative HR-TEM image of Pt/H-*BEA/4.2.

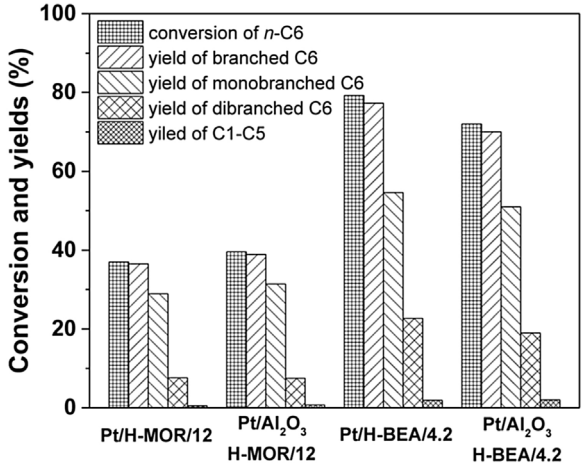

Fig. 8. Comparison of the conversions of *n*-hexane and the yields of branched C_6 isomers and C_1–C_5 by-products in the hydroisomerization reaction over *BEA and MOR catalysts with Pt introduced by a conventional incipient wetness impregnation (Pt/H-*BEA/4.2 and Pt/H-MOR/12) and the mechanical mixtures of the protonic form of zeolite and Pt/Al_2O_3 (H-*BEA/4.2-Pt/Al_2O_3 and H-MOR/12-Pt/Al_2O_3) at 225 °C. The reaction conditions same as in Fig. 6.

species, additional samples of Pt/H-MOR and Al-rich Pt/H-*BEA were prepared with the same concentration of platinum (1.5 wt.%) but differing in the form of Pt species and their distance from the acidic sites. The samples H-*BEA/5-Pt/Al_2O_3 and H-MOR/12-Pt/Al_2O_3 were prepared as mechanical mixtures of the protonic form of the irrespective zeolite and Pt/Al_2O_3. The Pt/Al_2O_3 was obtained using conventional incipient wetness impregnation of Al_2O_3 and subsequent calcination in air and reduction in hydrogen. The mixture was mixed to give a final Pt concentration of 1.5 wt.% and the resulting material was not calcined to preclude migration of Pt. Note that the hydroisomerization activity of resulting Pt/Al_2O_3 was negligible at a temperature up to 225 °C. Fig. 8 compares the yields of branched C_6 isomers and C_1–C_5 by-products over the catalysts obtained by a conventional incipient wetness impregnation and the mechanical mixtures of the H-zeolites and Pt/Al_2O_3 at 225 °C. It is obvious that the yields were practically identical for both the MOR samples, however, slightly lower for the H-*BEA/5-Pt/Al_2O_3 compared the Pt/H-*BEA/5. It indicates a minor role of the distance of Pt sites from the active acid sites on the activity of the Pt/H-*BEA/5. It indicates that the activity of the Al-rich Pt/H-*BEA is not connected with a specific Pt dispersion but the distance of Pt from the acid sites is important for the high activity of the Al-rich Pt/H-*BEA catalyst.

3.6. Implication of the enhanced activity of Al-rich Pt/H-*BEA on isomerization of n-hexane

It is well established that mordenite zeolites with strongly acidic bridging Si-OH-Al sites are the most active and selective among all the types of investigated zeolitic hydroisomerization catalysts [3,13,14,17,67,68]. However, considerably lower activity of mordenite zeolites compared to chlorinated alumina necessitates isomerization at higher temperatures leading to unfavorable thermodynamic equilibrium for branched isomers. An essential solution of the problem lies in significant enhancement of the isomerization activity that enables reaching high conversions at lower temperatures in a favorable area of the thermodynamic equilibrium. The remarkable increase in the yield of branched isomers and an increase in the selectivity for the desired products limiting cracking reactions over Al-rich Pt/H-*BEA enables a shift of the operation window to lower temperatures. To analyze the potential of the Al-rich *BEA zeolite as an environmentally sustainable low/medium temperature hydroisomerization catalyst, the activity, selectivity and durability of Al-rich Pt/H-*BEA were compared with state-of-the-art microporous and micro-mesoporous mordenite zeolites under model reaction conditions and also the relevant conditions of the hydroisomerization process, i.e. at elevated pressure and at high concentrations of *n*-hexane in the reaction stream. The yields of branched hexane isomers and C_1–C_5 by-products as a function of temperature at low pressures of *n*-hexane compared for Al-rich Pt/H-*BEA/4.2 and microporous and micro-mesoporous Pt/H-mordenite zeolites are shown in Fig. 9. The distribution of the formed mono-branched isomers (2-methylpentane and 3-methylpentane) and di-branched isomers (2,2-dimethylbutane and 2,3-dimethyl butane) is listed in Table S1. The yield of branched isomers was approximately 7 times higher (at 175 °C) over Al-rich BEA than over MOR, while the yield of C_1–C_5 by-products was comparable or lower to that over mordenite catalysts. The performance of the mordenite catalysts was comparable to Si-rich *BEA catalysts.

The performance characteristics of Al-rich Pt/H-*BEA compared to Si-rich Pt/H-*BEA and MOR zeolites under elevated pressure and at high concentration of hexane in the hydrogen stream relevant to the catalytic processes are listed in Table 3. A threefold increase in the concentration of the active sites and the synergetic effect clearly resulted in the desired increase in activity and selectivity. The Al-rich Pt/H-*BEA/4.2 gives an isomer yield of 51.1% at a temperature of

Table 3
The yields of branched hexane isomers and lower molecular weight by-products for hydroisomerization of *n*-hexane analyzed under process-like conditions.

	PtH-BEA/4.2		PtH-BEA/12		PtH-MOR/12		PtH-MOR/10	
	200 °C	215 °C	200 °C	215 °C	200 °C	215 °C	200 °C	215 °C
$y_{\Sigma iso\text{-}C6}$ (%)	51.1	76.8	12.1	31.8	10.1	25.4	10.5	28.1
$y_{2MP+3MP}$ (%)	44.8	62.1	11.9	29.1	8.8	21.8	9.5	24.5
$y_{2,2DMB}$ (%)	1.5	6.7	0.08	1.5	0.32	1	0.95	0.95
$y_{2,3DMB}$ (%)	4.8	8	0.2	1.2	0.93	2.6	0.86	2.67
$y_{by\text{-}productsC1\text{-}C4}$ (%)	0.11	2.0	10.7	26.7	0.58	1.3	0.65	1.7

Reaction conditions: WHSV 0.7 h^{-1}, molar ratio H_2/n-C_6 6, pressure 10 bar.

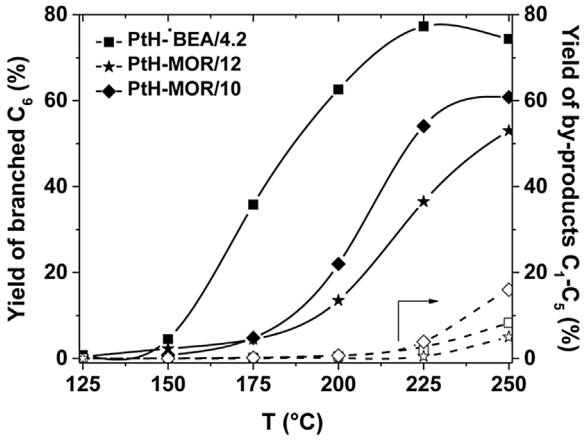

Fig. 9. Comparison of Al-rich *BEA (PtH-*BEA/4.2) with microporous PtH-MOR/12 and partially dealuminated micro-mesoporous PtH-MOR/10 zeolites in hydroisomerization of *n*-hexane. Effect of temperature on the yields of branched C_6 isomers and C_1–C_5 by-products. The reaction conditions same as in Fig. 6.

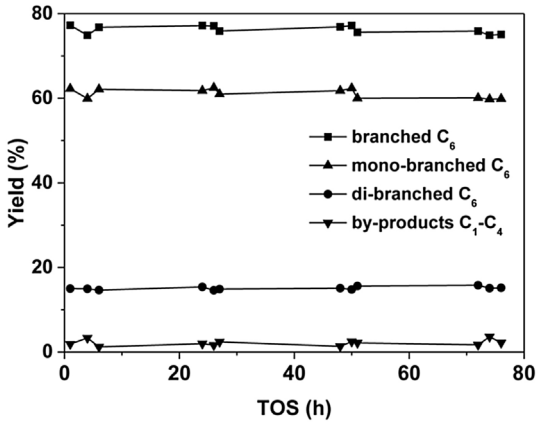

Fig. 10. Dependence of the yield of branched hexane isomers and C_1–C_4 by-products on time-on-stream in hydroisomerization of *n*-hexane over Al-rich *BEA (PtH-*BEA/4.2). Reaction conditions: Temperature 215 °C, WHSV 0.7 h^{-1}, molar ratio H_2/n-C_6 6, pressure 10 bar.

200 °C, whereas the Si-rich Pt/H-zeolites lead to isomers yields from 10.1 to 12.1% at the same temperature. Stable values of the yields of isomers ~74–77% and by-products ~2% as a function of time-on-stream were obtained at 215 °C for 76 h that indicates stability of the Al-rich Pt/H-*BEA (Fig. 10).

It is clear that the unique density and distribution of the strongly acidic sites are ultimately connected with catalytic performance highly exceeding that of state-of-the-art Si-rich zeolite catalysts. There is no evidence in the scientific literature that the strength of the acidity of the Al-rich H-*BEA zeolite is significantly weakened due to its high aluminum content, at least with respect to acid-catalysed transformations of hydrocarbons. On the contrary, acid-catalysed reactions requiring strongly acidic centers like alkylation and hydroamination of aromatics [33,58], and cracking and hydrocracking of aromatics and alkanes [27,29,33] are substantially improved over Al-rich H-*BEA exceeding significantly the Si-rich H-*BEA zeolites. Thus, the Al-rich H-*BEA provides the unique concentration of strongly acidic sites in the three-dimensional channel system with 12-MR openings. Such density of the acid sites is not available in zeolites with the three-dimensional channel system with 10-MR openings, e.g. MFI structural topology, due to the absence of a synthesis procedure for the preparation of zeolite with molar Si/Al ratio <10. Al-rich H-*BEA is also advantageous to Y zeolites, wherein the protonic sites are mutually affected due to the presence of Al-Si-Al sequences in the framework and exhibit much lower acid strengths [69]. The three-dimensional channel system with 12-MR openings of Al-rich H-*BEA is also a significant advantage over traditional mordenite based isomerization catalysts where the pseudo-monodimensional channel structure and the restricted accessibility of acid sites located in 8-MR channels limit the efficiency of the catalytic process by mass transfer effects [70].

The reduced apparent activation energy and increased TOF for Al-rich H-*BEA zeolite indicate only a partial contribution of the increased concentration of protonic sites to the overall enhancement of the catalytic properties and therefore another factor associated with the close proximity of the active sites plays an important role. Conversely, there are no spectroscopic signatures of significantly different acidic characteristics in the Al-rich beta zeolite. Because the enhancement of the strength of the acid groups has not been observed, the increase in specific activity of close non-interacting OH groups must be accompanied with another specific synergistic effect. Effects of the proximity of Brønsted and Lewis sites [71], the arrangement of acid centers influencing the entropy of the system or an interaction of one molecule with two close centers could possibly affect the overall catalytic process. However, we can not rule out that the overall increase in specific activity is given by contributions from others synergistic effects. The analysis of effects of the proximity of acid sites on reaction mechanism of skeletal isomerization of alkanes needs to be accessed in further studies to obtain full comprehending the consequences of the specific structure.

4. Conclusions

The critical function of the density of the acidic protons for hydroisomeroization of *n*-hexane was elucidated using the H-forms of the beta zeolites with a very high concentration of aluminum (Si/Al ≥ 4) with highly predominant tetrahedrally coordinated Al atoms in the framework. Analysis of the relationships between the density and distribution of strongly acidic sites and *n*-hexane isomerization identified a specific arrangement of Brønsted acid sites directing the reaction toward higher reaction rates. A high density of strongly acidic non-interacting close OH groups in the Al-rich H-*BEA zeolite (Si/Al ~ 4) lowers the activation barrier in the isomerization reaction and results in multiplying the reaction rates by

a factor of six compared to the hitherto most active Si-rich zeolite catalysts. The arrangement of Brønsted acid sites is unique for the Al-rich H-*BEA zeolite (Si/Al ~ 4) and is given by the arrangement of Al atoms in the Al-Si-Al sequences charge-balanced by two H^+ ions located in different zeolite channels. In conclusion, the achievement of the high concentration of non-interacting acidic protons in the zeolite catalyst allowed a significant increase in the isomerization activity and a shift of the operation temperature window into the thermodynamically more favourable region for desired di-branched isomers.

Acknowledgements

This work was supported by the Czech Science Foundation under project # 15-12113S and RVO: 61388955. The authors acknowledge the assistance provided by the Research Infrastructures NanoEnviCz and pro-NanoEnviCz, supported by the Ministry of Education, Youth and Sports of the Czech Republic under Project No. LM2015073.

Appendix A. Supplementary data

Supplementary data associated with this article can be found, in the online version, at http://dx.doi.org/10.1016/j.apcata.2016.12.016.

References

[1] E. Iglesia, S.L. Soled, G.M. Kramer, J. Catal. 144 (1993) 238–253.
[2] E. Iglesia, D.G. Barton, S.L. Soled, S. Miseo, J.E. Baumgartner, W.E. Gates, G.A. Fuentes, G.D. Meitzner, Stud. Surf. Sci. Catal. (1996) 533–542.
[3] A. Chica, A. Corma, J. Catal. 187 (1999) 167–176.
[4] Y. Ono, Catal. Today 81 (2003) 3–16.
[5] J. Macht, R.T. Carr, E. Iglesia, J. Am. Chem. Soc. 131 (2009) 6554–6565.
[6] R. Roldán, F.J. Romero, C. Jiménez-Sanchidrián, J.M. Marinas, J.P. Gómez, Appl. Catal. A 288 (2005) 104–115.
[7] W. Knaeble, R.T. Carr, E. Iglesia, J. Catal. 319 (2014) 283–296.
[8] M. Digne, P. Raybaud, P. Sautet, D. Guillaume, H. Toulhoat, J. Am. Chem. Soc. 130 (2008) 11030–11039.
[9] L. Gora, J.C. Jansen, J. Catal. 230 (2005) 269–281.
[10] H. Weyda, E. Köhler, Catal. Today 81 (2003) 51–55.
[11] A.N. Shakun, M.L. Fedorova, Catal. Ind. 6 (2014) 298–306.
[12] P. Sazama, Z. Sobalik, J. Dedecek, I. Jakubec, V. Parvulescu, Z. Bastl, J. Rathousky, H. Jirglova, Angew. Chem. Int. Ed. 52 (2013) 2038–2041.
[13] M. Tromp, J.A. van Bokhoven, M.T.G. Oostenbrink, J.H. Bitter, K.P. de Jong, D.C. Koningsberger, J. Catal. 190 (2000) 209–214.
[14] S.V. Konnov, I.I. Ivanova, O.A. Ponomareva, V.I. Zaikovskii, Microporous Mesoporous Mater. 164 (2012) 222–231.
[15] D.G. Barton, S.L. Soled, G.D. Meitzner, G.A. Fuentes, E. Iglesia, J. Catal. 181 (1999) 57–72.
[16] G.D. Yadav, J.J. Nair, Microporous Mesoporous Mater. 33 (1999) 1–48.
[17] H. Chiang, A. Bhan, J. Catal. 283 (2011) 98–107.
[18] W.O. Haag, R.M. Lago, P.B. Weisz, Nature 309 (1984) 589–591.
[19] A. Janda, A.T. Bell, J. Am. Chem. Soc. 135 (2013) 19193–19207.
[20] A.J. Jones, R.T. Carr, S.I. Zones, E. Iglesia, J. Catal. 312 (2014) 58–68.
[21] P. Sazama, J. Dedecek, V. Gabova, B. Wichterlova, G. Spoto, S. Bordiga, J. Catal. 254 (2008) 180–189.
[22] B. Xie, J. Song, L. Ren, Y. Ji, J. Li, F.S. Xiao, Chem. Mater. 20 (2008) 4533–4535.
[23] K. Shanjiao, D. Tao, L. Qiang, D. Aijun, Z. Yanying, P. Huifang, J. Porous Mater. 15 (2008) 159–162.
[24] G. Majano, L. Delmotte, V. Valtchev, S. Mintova, Chem. Mater. 21 (2009) 4184–4191.
[25] Y. Kamimura, W. Chaikittisilp, K. Itabashi, A. Shimojima, T. Okubo, Chem.—Asian J. 5 (2010) 2182–2191.
[26] Y. Kamimura, S. Tanahashi, K. Itabashi, A. Sugawara, T. Wakihara, A. Shimojima, T. Okubo, J. Phys. Chem. C 115 (2011) 744–750.
[27] B. Xie, H. Zhang, C. Yang, S. Liu, L. Ren, L. Zhang, X. Meng, B. Yilmaz, U. Muller, F.-S. Xiao, Chem. Commun. (Cambridge U. K.) 47 (2011) 3945–3947.
[28] K. Itabashi, Y. Kamimura, K. Iyoki, A. Shimojima, T. Okubo, J. Am. Chem. Soc. 134 (2012) 11542–11549.
[29] T. De Baerdemaeker, B. Yilmaz, U. Muller, M. Feyen, F.S. Xiao, W. Zhang, T. Tatsumi, H. Gies, X. Bao, D. De Vos, J. Catal. 308 (2013) 73–81.
[30] H. Zhang, B. Xie, X. Meng, U. Mueller, B. Yilmaz, M. Feyen, S. Maurer, H. Gies, T. Tatsumi, X. Bao, W. Zhang, D. De Vos, F.-S. Xiao, Microporous Mesoporous Mater. 180 (2013) 123–129.
[31] Y. Kubota, K. Itabashi, S. Inagaki, Y. Nishita, R. Komatsu, Y. Tsuboi, S. Shinoda, T. Okubo, Chem. Mater. 26 (2014) 1250–1259.
[32] B. Zheng, Y. Wan, W. Yang, F. Ling, H. Xie, X. Fang, H. Guo, Chin. J. Catal. 35 (2014) 1800–1810.
[33] P. Sazama, B. Wichterlova, S. Sklenak, V.I. Parvulescu, N. Candu, G. Sadovska, J. Dedecek, P. Klein, V. Pashkova, P. Stastny, J. Catal. 318 (2014) 22–33.
[34] R.B. Borade, A. Clearfield, Chem. Commun. (Cambridge, U. K.) (1996) 625–626.
[35] B. Wichterlova, Z. Tvaruzkova, Z. Sobalik, P. Sarv, Microporous Mesoporous Mater. 24 (1998) 223–233.
[36] C.A. Fyfe, Y. Feng, H. Grondey, G.T. Kokotailo, H. Gies, Chem. Rev. (Washington DC, U. S.) 91 (1991) 1525–1543.
[37] G. Engelhardt, U. Lohse, E. Lippmaa, M. Tarmak, M. Magi, Z. Anorg, Allg. Chem. 482 (1981) 49–64.
[38] A. Van De Runstraat, J.A. Kamp, P.J. Stobbelaar, J. Van Grondelle, S. Krijnen, R.A. Van Santen, J. Catal. 171 (1997) 77–84.
[39] W.O. Haag, R.M. Lago, P.B. Weisz, Faraday Discuss. Chem. Soc. 72 (1981) 317–330.
[40] M. Muller, G. Harvey, R. Prins, Microporous Mesoporous Mater. 34 (2000) 135–147.
[41] H. Huo, L. Peng, Z. Gan, C.P. Grey, J. Am. Chem. Soc. 134 (2012) 9708–9720.
[42] P. Strodel, K.M. Neyman, H. Knozinger, N. Rosch, Chem. Phys. Lett. 240 (1995) 547–552.
[43] M. Sigl, S. Ernst, J. Weitkamp, H. Knozinger, Catal. Lett. 45 (1997) 27–33.
[44] I. Kiricsi, C. Flego, G. Pazzuconi, W.O. Parker, R. Millini, C. Perego, G. Bellussi, J. Phys. Chem. 98 (1994) 4627–4634.
[45] J. Brus, L. Kobera, W. Schoefberger, M. Urbanová, P. Klein, P. Sazama, E. Tabor, S. Sklenak, A.V. Fishchuk, J. Dedecek, Angew. Chem. Int. Ed. 54 (2015) 541–545.
[46] P. Sazama, B. Wichterlova, J. Dedecek, Z. Tvaruzkova, Z. Musilova, L. Palumbo, S. Sklenak, O. Gonsiorova, Microporous Mesoporous Mater. 143 (2011) 87–96.
[47] E. Bourgeat-Lami, P. Massiani, F. Di Renzo, P. Espiau, F. Fajula, T. Des Courieres, Appl. Catal. 72 (1991) 139–152.
[48] L.W. Beck, J.F. Haw, J. Phys. Chem. 99 (1995) 1076–1079.
[49] L.C. De Menorval, W. Buckermann, F. Figueras, F. Fajula, J. Phys. Chem. 100 (1996) 465–467.
[50] P.J. Kunkeler, B.J. Zuurdeeg, J.C. Van Der Waal, J.A. Van Bokhoven, D.C. Koningsberger, H. Van Bekkum, J. Catal. 180 (1998) 234–244.
[51] G.H. Kuehl, H.K.C. Timken, Microporous Mesoporous Mater. 35-36 (2000) 521–532.
[52] J. Penzien, A. Abraham, J.A. Van Bokhoven, A. Jentys, T.E. Muller, C. Sievers, J.A. Lercher, J. Phys. Chem. B 108 (2004) 4116–4126.
[53] P. Sazama, E. Tabor, P. Klein, B. Wichterlova, S. Sklenak, L. Mokrzycki, V. Pashkkova, M. Ogura, J. Dedecek, J. Catal. 333 (2016) 102–114.
[54] J.R. Anderson, Y.F. Chang, R.J. Western, J. Catal. 118 (1989) 466–482.
[55] M. Bjørgen, F. Bonino, S. Kolboe, K.P. Lillerud, A. Zecchina, S. Bordiga, J. Am. Chem. Soc. 125 (2003) 15863–15868.
[56] M. Ma, K.E. Johnson, J. Am. Chem. Soc. 117 (1995) 1508–1513.
[57] K. Hemelsoet, Q. Qian, T. De Meyer, K. De Wispelaere, B. De Sterck, B.M. Weckhuysen, M. Waroquier, V. Van Speybroeck, Chem. Eur. J. 19 (2013) 16595–16606.
[58] B. Yilmaz, U. Muller, M. Feyen, S. Maurer, H. Zhang, X. Meng, F.S. Xiao, X. Bao, W. Zhang, H. Imai, T. Yokoi, T. Tatsumi, H. Gies, T. De Baerdemaeker, D. De Vos, Catal. Sci. Technol. 3 (2013) 2580–2586.
[59] Y. Sasaki, Y. Yoshida, C.A.J. Fisher, T. Ikeda, K. Itabashi, T. Okubo, Microporous Mesoporous Mater. 225 (2016) 210–215.
[60] P. Sazama, L. Mokrzycki, B. Wichterlova, A. Vondrova, R. Pilar, J. Dedecek, S. Sklenak, E. Tabor, J. Catal. 332 (2015) 201–211.
[61] P. Sazama, R. Pilar, L. Mokrzycki, A. Vondrova, D. Kaucky, J. Plsek, S. Sklenak, P. Stastny, P. Klein, Appl. Catal. B 189 (2016) 65–74.
[62] S. Suganuma, H. Zhang, C. Yang, F.S. Xiao, N. Katada, J. Porous Mater. 23 (2016) 415–421.
[63] F. Ribeiro, C. Marcilly, M. Guisnet, J. Catal. 78 (1982) 267–274.
[64] A.Y. Stakheev, E.S. Shpiro, O.P. Tkachenko, N.I. Jaeger, G. Schulz-Ekloff, J. Catal. 169 (1997) 382–388.
[65] P. Kubanek, H.W. Schmidt, B. Spliethoff, F. Schüth, Microporous Mesoporous Mater. 77 (2005) 89–96.
[66] R. Monteiro, C.O. Ania, J. Rocha, A.P. Carvalho, A. Martins, Appl. Catal. A 476 (2014) 148–157.
[67] K.J. Chao, H.C. Wu, L.J. Leu, Appl. Catal. A 143 (1996) 223–243.
[68] N. Viswanadham, L. Dixit, J.K. Gupta, M.O. Garg, J. Mol. Catal. A Chem. 258 (2006) 15–21.
[69] N. Wang, M. Zhang, Y. Yu, Microporous Mesoporous Mater. 169 (2013) 47–53.
[70] M. Tromp, J.A. van Bokhoven, M.T. Garriga Oostenbrink, J.H. Bitter, K.P. de Jong, D.C. Koningsberger, J. Catal. 190 (2000) 209–214.
[71] J.A. Van Bokhoven, B.A. Williams, W. Ji, D.C. Koningsberger, H.H. Kung, J.T. Miller, J. Catal. 224 (2004) 50–59.